IEEE Open Journal of
Antennas and Propagation

Received 4 September 2023; revised 20 October 2023; accepted 29 October 2023. Date of publication 6 November 2023; date of current version 1 December 2023.

Digital Object Identifier 10.1109/OJAP.2023.3330438

Efficient Calibration of Colocated MIMO Radar

RICARD L. GROVE [1,2] AND JØRGEN DALL [1] (Member, IEEE)

[1]National Space Institute, Technical University of Denmark (DTU), 2800 Kongens Lyngby, Denmark

[2]Technology Department, Weibel Scientific A/S, 3450 Allerød, Denmark

CORRESPONDING AUTHOR: J. DALL (e-mail: jd@space.dtu.dk)

This work was supported by the Thomas B. Thriges Foundation.

ABSTRACT Measurement-based calibration with a complete MIMO radar system is beneficial due to all imperfections being considered simultaneously. However, if high performance is needed, the number of required calibration measurements escalates with an increasing number of antenna elements. This paper presents a calibration technique that reduces the number of measurements required to obtain adequate calibration coefficients, compensating for all system imperfections that can be described in matrix form. This includes channel imbalance and mutual coupling under the assumption of minimum scattering antennas. The proposed technique estimates the calibration matrix for the transmit and receive array separately, by canceling out the element radiation pattern and effects from the other array through normalization. In this way, the computational complexity and the risk of local convergence is reduced. Using prior knowledge of the expected mutual coupling, the number of equations in the nonlinear least-squares can be further reduced without affecting the calibration performance. Besides validation with a simulated model, the calibration technique is applied to an eight-by-eight MIMO radar system.

INDEX TERMS Colocated multiple-input multiple-output (MIMO) radar, array calibration, channel imbalance, mutual coupling, digital beamforming.

I. INTRODUCTION

COMBINING each transmit antenna element with all receive elements, the multiple-input multiple-output (MIMO) radar forms a larger virtual array with a number of elements equal to the product of transmit and receive elements. With appropriate positioning of the colocated physical antennas, continuous observation with an increased angle resolution can be obtained within a large field-of-view (FOV) only limited by the element radiation pattern [1], [2], [3]. These properties have led to intensive research and development of MIMO radars for imaging, especially in the automotive sector [4], [5], [6], but also for air surveillance of, for instance, drones [7], [8].

The MIMO radar virtual array structure plays a significant role when investigating the system imperfection effects on the system performance, as each physical element is represented repeatedly. As a consequence, if channel imbalances occur due to, for instance, differences from the RF components or signal path length, they are repeated across the virtual array as documented in [9], [10]. Interactions between the antenna elements, i.e., mutual coupling, result in the embedded radiation pattern causing angle-dependent imperfection effects. The impact of mutual coupling increases when the element environment is not geometrically symmetric, which is the case for the end elements. Hence, the consequence of mutual coupling is typically more significant at large angles [11], [12], [13]. These effects leave an uncalibrated MIMO radar system vulnerable to severe performance degradation in the azimuth dimension referred to as the beam pattern. Naturally, calibration is necessary for obtaining a well-focused beam pattern and, hereby, correctly estimating the direction-of-arrival (DOA) of potential targets in the scene.

Compensation can be performed by characterizing each source of system imperfections manually. Channel imbalance calibration can, with reasonable accuracy, be achieved by implementing internal calibration loops [14], [15]. In addition, the mutual coupling matrix is commonly used to model system imperfections arising from the interactions between the elements in the antenna array. They can be

estimated by measuring the mutual impedance of the antenna array [16], which is applied to a MIMO radar system in [17]. However, this procedure is cumbersome and impossible for most systems on a chip.

Instead, measurement-based calibration is preferred, where the entire system and all the imperfection contributions are combined. An extensively used calibration technique is to conduct a single measurement of a calibration target and compute the deviation between measured and expected signal [4], [18]. Hereby, all imperfections for each virtual element at the given angle are efficiently estimated within a narrow angular span. However, a wide FOV is typically desired for a MIMO radar system, and the performance quickly deteriorates for larger angles relative to the angle of the calibration target.

To accommodate for the angle-dependent effects on the beam pattern of mutual coupling, a series of measurements is needed at well-defined angles. The straightforward solution is to average the channel imbalance coefficients at different angles such that the average mutual coupling effects are estimated [19]. Alternatively, the mutual coupling matrix can be estimated through a linear least squares solution as described for an antenna array in [20], [21], [22]. The technique has been implemented for the MIMO radar as well by estimating the mutual coupling matrix of the virtual array [23], [24]. However, the number of parameters to be estimated are in the same order of magnitudes as the number of virtual elements. Consequently, for larger arrays in particular, the number of required calibration measurements escalates.

Latest, new calibration techniques are described where the transmit and receive arrays are separated when estimating the mutual coupling matrix. This leads to a reduction of the number of required calibration measurement, which is usually desirably. In [25], an iterative method is described, where the transmit and receive arrays are alternately optimized by using the previous estimate of the other array. However, as the optimization is performed on biased coefficients of the other array, the dependency between the arrays can lead to increased risk of local rather than global convergence for a non-convex problem. In [26], the transmit and receive arrays are separated with a singular vector decomposition. It is based on the assumption that the steering vectors of the transmit and receive arrays are the left and right singular values, respectively.

Unlike [25] and [26], the proposed calibration technique handles the transmit array completely independently from the receive array and vice versa. Elimination of the imperfections originating from the opposite array is achievable by exploiting matrix multiplication properties and normalization. This reduces the computational complexity and the risk of local convergence. Moreover, the normalization eliminates the effects of the isolated element pattern, which would otherwise affect the amplitude coefficients. Finally, the proposed calibration technique unlocks the possibility of further reducing the number of parameters by omitting coupling coefficients that theoretically can be negligible due to sizable inter-element spacing. With the physical geometry better represented in the model, the number of necessary measurements, Q, is reduced, and a higher performance is achieved while drastically reducing the computational complexity of the parameter estimation.

The paper is organized into the following sections: In Section II, the signal model describing a MIMO radar system including imperfections is presented along with the model assumptions. It forms the background for our proposed calibration technique presented in Section III. Its performance is demonstrated under the ideal conditions of a simulation environment in Section IV and compared to a selection of other calibration techniques. Similarly, in Section V the techniques are applied to a set of data collected with a physical MIMO radar system outlined in [27], before concluding the paper in Section VI.

II. SIGNAL MODEL

The signal model presented in this paper represents a calibration setup of a MIMO radar system. In the following, assumptions applicable to the signal model are described, and substantiated experimentally in Section V:

a) The far-field approximation, which assumes the signal across an aperture can be described by a planar wave. This implies that the DOA, θ_0, i.e., the direction of a target relative to the array boresight, is identical for all antenna elements. Under a controlled setup where the distance and DOA is known, a near-field correction can be applied instead of assuming that the far-field approximation is valid.

b) The calibration target is a single point target, for instance, a corner reflector. In addition, it is assumed that the radar cross-section of the target is the same seen by all antenna elements.

c) Unwanted signals that inevitably are present in a measurement environment are assumed negligible; clutter and multipath propagation can typically be reduced by performing the measurements in an anechoic chamber. Otherwise, clutter subtraction is needed. In addition, the direct coupling between the transmit and receive elements can be filtered out through range-gating, as the signal appears at a near-zero range.

d) The transmitted signals are fully orthogonal, which is obtained by concentrating their cross-correlations into well-defined grating lobes in either the range or Doppler domain by time- or Doppler-division multiplexing, respectively [28]. The impact of mutual coupling in a MIMO radar is presented for a selection of phase-coded waveforms in [17].

e) Identical antennas are used for all array elements, and reciprocity is assumed such that the transmit and receive properties of the elements are identical. In addition, it is assumed that the antennas and the related hardware have negligible characteristic variations within the entire frequency band.

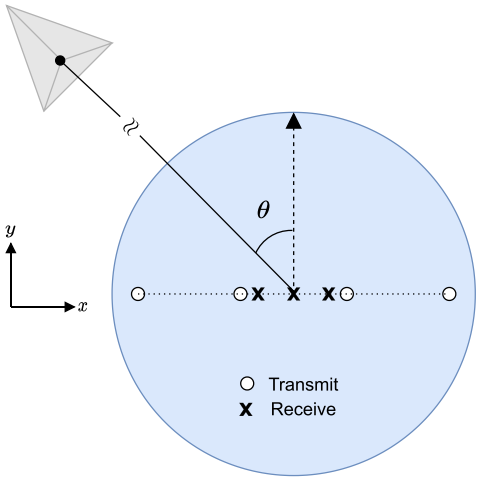

FIGURE 1. Geometry of calibration setup of a linear MIMO array with four transmit elements and three receive elements. The virtual array midpoint is located at the turn table origin.

f) The MIMO array consists of minimum scattering antennas (MSA) [29]. Hereby, the antenna mutual coupling only affects the phase and amplitude of the current distribution but not its shape. Consequently, the embedded radiation pattern of each element can be described as superimposed contributions of the isolated element pattern defined by a scattering matrix. As a result, the coupling can be described as a linear and angle-independent coupling matrix, $\mathbf{C}$. However, most antennas are not MSAs [30]. For phased-array radars, the problem of non-MSAs is circumvented as the active radiation pattern is estimated for each scanning angle [31], [32], [33]. In general, colocated MIMO radar systems aim to continuously cover a large FOV, and the technique is not applicable. Hence, the MSA approximation is widely adopted when calibrating MIMO radar systems, e.g., [17], [19], [20], [21], [22], [23], [24]. Increased calibration performance can be obtained by applying an angle-dependent coupling matrix, $\mathbf{C}(\theta)$, such as in [34]. The downside is additional computational complexity, as prior knowledge of the target DOA is needed for optimal performance. Moreover, the calibration does not support multiple targets at different angles in the same range and Doppler-cell.

g) For a calibration setup, several measurements of the same target are to be conducted at different angles, which can be obtained efficiently by placing the MIMO radar on a turntable. This paper assumes that the virtual array midpoint is located at the turntable origin. An offset can be modeled as in [25], however, the proposed calibration technique bypasses the error contribution through normalization as described in Section III. Consequently, the measurement setup is equivalent to having a fixed antenna setup and moving the calibration target as shown geometrically in Fig. 1.

Obviously, these assumptions apply to a system that is not engaged. The same assumptions apply to the majority of the published calibration methods, whereas different assumptions apply to auto-calibration techniques, where especially the effects in assumption c), would call for a compensation.

Together with assumptions a)-d), the ideal collected signal can be reduced to a steering matrix. It describes the propagation from each transmitter to every receiver relative to a reference point located anywhere on the virtual array, but typically at the array center:

$$\begin{aligned}\mathbf{P}(\theta) &= \exp\left[-jk\sin(\theta)\boldsymbol{d}_r^T\right]\exp\left[-jk\sin(\theta)\boldsymbol{d}_t\right]\\ &= \begin{bmatrix} p_{r,1}(\theta) \\ \vdots \\ p_{r,N_r}(\theta)\end{bmatrix}\left[p_{t,1}(\theta)\ \cdots\ p_{t,N_t}(\theta)\right],\end{aligned} \tag{1}$$

where $p_{t,m}(\theta)$ and $p_{r,n}(\theta)$ describe the propagation coefficients from the transmit and receive array, respectively, $\exp[\cdot]$ denotes the element-wise exponential, k the wavenumber, the superscript T is the matrix transpose, while $\boldsymbol{d}_t$ and $\boldsymbol{d}_r$ are the distances from the reference point to the transmit and receive element positions, respectively:

$$\boldsymbol{d}_t = \left[d_{t,1}\ \ldots\ d_{t,N_t}\right] \tag{2a}$$
$$\boldsymbol{d}_r = \left[d_{r,1}\ \ldots\ d_{r,N_r}\right]. \tag{2b}$$

Here, N_t and N_r are the numbers of transmit and receive elements, respectively, such that $\mathbf{P}(\theta)$ is an $N_r \times N_t$ matrix.

Including the element radiation patterns under isolated conditions together with the two-way propagation effects from the reference point expands (1) to

$$\mathbf{S}(r,\theta) = \mathbf{E}_r(\theta)\mathbf{P}(\theta)\mathbf{E}_t(\theta)P_{ref}(r,\theta), \tag{3}$$

where $\mathbf{E}_\alpha(\theta)$ with $\alpha \in [t, r]$ is the diagonal square matrix of order N_α containing the element pattern of each element, $e(\theta)$, and $P_{ref}(r,\theta)$ is the complex factor describing the two-way propagation phase and loss from the array reference point with r denoting the range to the target. Applying assumption e) (3) can be reduced to

$$\mathbf{S}(r,\theta) = \mathbf{P}(\theta)e(\theta)^2P_{ref}(r,\theta), \tag{4}$$

which describes the ideal system without imperfections. The isolated element pattern can typically be estimated with high accuracy from a full-wave simulation if enough knowledge of the array is available. In this paper, it is assumed unknown. Next, system imperfections are included. They can be grouped into channel imbalance and mutual coupling. However, for measurement-based calibration, all imperfections of each array are contained in a single complex square matrix, $\mathbf{C}_\alpha$, of order N_α, where the diagonal and off-diagonal describe the channel imbalance and mutual coupling coefficients, respectively. Under assumption f), the collected signals including system imperfections become

$$\mathbf{X}(r,\theta) = \mathbf{C}_r\mathbf{S}(r,\theta)\mathbf{C}_t + \mathbf{W} \tag{5}$$

where $\mathbf{W}$ is an $N_r \times N_t$ matrix representing the noise components which are assumed to be Gaussian white noise. For the system calibration, the scene, i.e., the expected signal return, $\mathbf{S}(r,\theta)$, is well-known, and the system imperfections described by $\mathbf{C}_\alpha$ are to be estimated. For a system without imperfections, $\mathbf{C}_\alpha = \mathbf{I}_\alpha$, which is the identity matrix of order N_α. From the estimated imperfection matrices, $\hat{\mathbf{C}}_\alpha$, the system can be calibrated by

$$\hat{\mathbf{S}}(r,\theta) = \hat{\mathbf{C}}_r^{-1}\mathbf{X}(r,\theta)\hat{\mathbf{C}}_t^{-1} \tag{6}$$

given that the $\mathbf{C}_\alpha$ matrices are not ill-conditioned. However, diagonally dominated matrices, such as the imperfection matrices, $\mathbf{C}_\alpha$, are typically well-conditioned.

III. PROPOSED CALIBRATION ALGORITHM

The proposed calibration algorithm description is split into three parts: Isolation of the transmit and receive array, nonlinear least squares estimation, and finally, reduction of the number of model parameters. Throughout the description, the noise will be omitted and instead be discussed separately in Section IV-D.

A. ISOLATION OF TRANSMIT AND RECEIVE ARRAY

From (5), the measured signal consists of superimposed contributions from both arrays simultaneously. The combined effect of the array imperfections will impact the ideal signal differently across the azimuth dimension. In addition, the isolated element pattern also affects the return signal with respect to θ_0. In [25], this is considered by including both imperfection matrices in the least squares problem formulation. However, exploiting some properties of the MIMO steering matrix makes it possible to isolate the receive and transmit array contributions entirely, reducing the computational complexity.

By omitting for a moment the element pattern and the propagation reference for convenience, the collected signals in (5) can be expanded to:

$$\mathbf{X}(\theta) = \mathbf{C}_r \begin{bmatrix} p_{r,1}(\theta) \\ \vdots \\ p_{r,N_r}(\theta) \end{bmatrix} \begin{bmatrix} p_{t,1}(\theta) & \cdots & p_{t,N_t}(\theta) \end{bmatrix} \mathbf{C}_t, \tag{7}$$

and by defining the matrix multiplication between the steering vector and mutual coupling matrices of the transmit and receive arrays separately, (7) can be further rewritten as

$$\mathbf{X}(\theta) = \begin{bmatrix} c_{rp,1}(\theta) \\ \vdots \\ c_{rp,N_r}(\theta) \end{bmatrix} \begin{bmatrix} c_{pt,1}(\theta) & \cdots & c_{pt,N_t}(\theta) \end{bmatrix}, \tag{8}$$

where all receive imperfections of receiver n are described by

$$c_{rp,n}(\theta) = p_{r,1}(\theta)r_{n,1} + \cdots + p_{r,N_r}(\theta)r_{n,N_r}, \tag{9}$$

with $r_{n,m}$ corresponding to the nmth element of $\mathbf{C}_r$. Equivalently, all transmit imperfections of transmitter m are described by

$$c_{pt,m}(\theta) = p_{t,1}(\theta)t_{1,m} + \cdots + p_{t,N_t}(\theta)t_{N_t,m}. \tag{10}$$

where $t_{n,m}$ equivalently corresponds to the nmth element of $\mathbf{C}_t$.

1) RECEIVE ARRAY

A consequence of $\mathbf{P}(\theta)$ being the outer product of two vectors is that the impact of the transmit imperfections is the same for all elements of a column in (8). Reintroducing the embedded element pattern and propagation reference, the first column of $\mathbf{X}(\theta)$ becomes:

$$\boldsymbol{x}_{*1}(\theta) = \begin{bmatrix} c_{rp,1}(\theta)c_{pt,1}(\theta)e(\theta)^2P_{ref}(r,\theta) \\ \vdots \\ c_{rp,N_r}(\theta)c_{pt,1}(\theta)e(\theta)^2P_{ref}(r,\theta) \end{bmatrix}, \tag{11}$$

where $(*)$ denotes all elements of the given matrix dimension.

As all transmit imperfections, the element radiation pattern and the propagation reference are identical for all elements in (11) cf. assumption e), these variables can be eliminated by normalizing with the first element, leaving $N_r - 1$ equations with N_r^2 model parameters:

$$\begin{aligned} \boldsymbol{x}'_{*1}(\theta) &= \boldsymbol{x}_{*1}(\theta)/x_{11}(\theta) \\ &= \begin{bmatrix} 1 \\ \frac{c_{rp,2}(\theta)}{c_{rp,1}(\theta)} \\ \vdots \\ \frac{c_{rp,N_r}(\theta)}{c_{rp,1}(\theta)} \end{bmatrix}. \end{aligned} \tag{12}$$

To acquire more equations than model parameters, the minimum number of measurements, Q_{min}, is:

$$(N_r - 1)Q_{min} > N_r^2 \Rightarrow Q_{min} = N_r + 2 \tag{13}$$

The normalization eliminates $P_{ref}(r,\theta)$, hence the dependency on the distance between the calibration target and the reference element, but the noise is amplified by the normalization, in particular in directions where $e(\theta)$ is small. The noise amplification is addressed in Section IV-D.

The receive coefficients from (12) are solely estimated from the signal originating from the first transmitter. Hence, the procedure can be repeated for every column, estimating the receive array coefficients N_t times, thereby increasing the model robustness. Implementing this feature does not provide additional information on the angular dependency of the system. Hence, the additional equations only increase robustness but not the minimum number of required measurements for coefficient estimation.

2) TRANSMIT ARRAY

In the same manner, the transmit array imperfections can be isolated. Opposite to the transmit array, the impact of the receive imperfections is the same for all elements of a row in (8). For instance, the first row of $\mathbf{X}(\theta)$ is:

$$\boldsymbol{x}_{1*}(\theta) = \begin{bmatrix} c_{rp,1}(\theta)c_{pt,1}(\theta)e(\theta)^2P_{ref}(r,\theta) \\ \vdots \\ c_{rp,1}(\theta)c_{pt,N_t}(\theta)e(\theta)^2P_{ref}(r,\theta) \end{bmatrix}^T, \tag{14}$$

After normalization with the first element in (14), the radiation pattern and receive imperfections cancel out, leaving only the coefficients of the transmit array:

$$\boldsymbol{x}'_{1*}(\theta) = \boldsymbol{x}_{1*}(\theta)/x_{11}(\theta) = \begin{bmatrix} 1 \\ \frac{c_{pt,2}(\theta)}{c_{pt,1}(\theta)} \\ \vdots \\ \frac{c_{pt,N_t}(\theta)}{c_{pt,1}(\theta)} \end{bmatrix}^T. \tag{15}$$

As with the receive array, an increased robustness can be achieved by repeating the procedure for the N_r rows.

B. NONLINEAR LEAST SQUARES ESTIMATION

Another effect of the normalization is that the model problem formulation is not linear. Instead, a nonlinear least squares technique is used, namely the Levenberg-Marquardt Method (LM). The technique minimizes the sum of squares of a set of nonlinear functions, f, with the model parameters β:

$$\mathbf{F}(\beta) = \frac{1}{2}\sum_{i=1}^{L}\left[f_i(\beta)\right]^2 \tag{16}$$

with L being the total number of functions. The calibration technique proposed in this paper estimates the receive and transmit coefficients independently using (12) and (15), respectively, as input equations to (16). Including all possible equations, the set of equations for the receive array becomes

$$\boldsymbol{f}(\mathbf{C}_r) = \begin{bmatrix} \boldsymbol{x}'_{*1}(\mathbf{C}_r, \theta_1) - \boldsymbol{p}_{*1}(\theta_1) \\ \vdots \\ \boldsymbol{x}'_{*N_t}(\mathbf{C}_r, \theta_1) - \boldsymbol{p}_{*N_t}(\theta_1) \\ \boldsymbol{x}'_{*1}(\mathbf{C}_r, \theta_2) - \boldsymbol{p}_{*1}(\theta_2) \\ \vdots \\ \boldsymbol{x}'_{*N_t}(\mathbf{C}_r, \theta_Q) - \boldsymbol{p}_{*N_t}(\theta_Q) \end{bmatrix} \tag{17}$$

where $\boldsymbol{p}_{*n_t}(\theta_q)$ is the n_tth column of $\mathbf{P}(\theta_q)$, normalized with respect to the first element of measurement q with $q \in [1, Q]$. In principle, every N_rth equation in (17) does not provide any valuable information as $\boldsymbol{x}'_{1*} = \boldsymbol{p}_{1*} = 1$, and they can be omitted. Thus, a total of $Q(N_r - 1)N_t$ equations are used for the estimation of the N_r^2 coefficients. In addition, there is a trade-off between computational complexity and model robustness: The N_t equations for each measurement increase the model robustness against noise but also the complexity without adding any information about the system angle-dependency.

The set of equations for the transmit array would be equivalent to (17), except for the usage of (14) and the corresponding steering matrix coefficients.

Denoting the Jacobian of $f_i(\beta)$ by $\mathbf{J}_i(\beta)$, the problem formulation of the LM method at each iteration, j, becomes

$$\left(\mathbf{J}(\beta_j)^T\mathbf{J}(\beta_j) + \Lambda_j\mathbf{I}\right)\rho_j = -\mathbf{J}(\beta_j)^T\boldsymbol{f}(\beta_j) \tag{18}$$

with Λ being the damping parameter and ρ being the search direction. The damping parameter determines the size of each step in the given search direction, and hereby, regulates how fast $\mathbf{F}$ is minimized. In addition, the initial damping can be manually selected, and if the iterative solution converges Λ should be gradually reduced. Several stop criteria are possible for iterative techniques. In this paper, the stop criterion is defined by the relative step size between two iterations;

$$|\hat{\mathbf{C}}_{\alpha,i} - \hat{\mathbf{C}}_{\alpha,i+1}| < \epsilon\left(1 + |\hat{\mathbf{C}}_{\alpha,i}|\right) \tag{19}$$

where the tolerance is set to $\epsilon = 1\mathrm{e}^{-6}$.

Finally, LM requires an initial guess for the calibration matrices which are set to $\hat{\mathbf{C}}_{\alpha 0} = \mathbf{I}_\alpha$, corresponding to the ideal case without imperfections.

C. REDUCTION OF MODEL PARAMETERS

Writing up the set of equations to be minimized gives the possibility to reduce the number of model parameters. If some coefficients in the model are sufficiently small to be neglected, they can be omitted from the equations. This is in particular of interest for the coupling between elements that are physically located far away from each other with respect to the wavelength.

Doing so has the benefit of reducing the model complexity. Naturally this does not only reduce the computational complexity, but, more importantly, the number of measurements needed to estimate the calibration coefficients, Q_{min}. In addition, the model would better represent the physical behavior of the system, such that near-zero coefficients do not model noise, which will be demonstrated later.

The number of coefficients that can be disregarded is highly dependent on the system; The number of channels, the antenna characteristics, and their relative positions.

IV. SIMULATION VERIFICATION

A MIMO radar system, including imperfections, is simulated to verify the proposed calibration technique.

A. SIMULATION SETUP

The simulated system is designed to resemble the demonstrator used for experimental verification in Section V. Hence, the system consists of 8×8 antennas with $\lambda/2$ and 4λ spacing between the receive and transmit elements, respectively, with λ being the wavelength of the carrier frequency. Hereby, a 64-element virtual uniform linear array (ULA) is formed without producing any grating lobes.

In contrast to data measured with a physical system, the simulation environment can be fully controlled. Hence, all assumptions in a simulation environment, as described in the signal model, are legitimate. This also implies that the target is infinitely far away such that the phases are only affected by the angle of the target. The element radiation pattern is modelled by

$$e(\theta) = \cos(\theta) \tag{20}$$

and the antennas are assumed to be MSAs. The mutual coupling coefficients are described by a full-wave simulation of open-ended waveguides [27]. The channel imbalance is modelled as an uncorrelated normal distribution of the real and imaginary components with zero mean and a standard deviation of -14 dB relative to the ideal normalized signal.

Two data sets are then generated with targets located at $\theta_0 = [-80°, 80°]$ and an angle separation of one degree. The first data set will be referred to as the training set, where calibration coefficients are estimated. They are afterwards applied to the second data set, the validation set, from which two performance parameters are estimated; the peak sidelobe level (PSL) and angle error. PSL gives an indication of the probability of false alarm due to the imperfection errors, while the angle error indicates the accuracy of the direction to a target. Uncorrelated white Gaussian noise is added to both data sets with an SNR of 30 dB after range and Doppler processing, which can usually be achieved with a physical system by having a strong reflector in the radar proximity. To investigate the calibration performance with respect to the number of calibration measurements, a series of calibration coefficients are estimated from an equidistantly spaced selection of the training set data in the full angle interval $\pm 80°$. The number of calibration measurements ranges from $Q \in [3, 161]$, and, for instance, at $Q = 3$ the angles used are $\theta_0 = -80°, 0°, 80°$. Hence, a total of 159 sets of calibration coefficients are estimated.

B. CALIBRATION TECHNIQUES FOR COMPARISON

To better validate the proposed method, the following previously presented calibration techniques are used for comparison:

1) *Virtual Element Averaging (VAV):* The residual between measured and expected data is averaged instead of modelled for all virtual elements across the given calibration measurements [19]. Consequently, all imperfections are combined into a single calibration coefficient for each channel, i.e., the imperfection matrix becomes a diagonal matrix.
2) *Virtual Element Least Squares (VLS):* The least squares technique of an antenna array adopted to the MIMO array [23]. This can be achieved by simply rewriting (5) as

$$\text{vec}(\mathbf{X}(\theta)) = \mathbf{C}_v \text{vec}(\mathbf{S}(\theta)) + \text{vec}(\mathbf{W}) \tag{21}$$

where

$$\mathbf{C}_v = \mathbf{C}_t^T \otimes \mathbf{C}_r \tag{22}$$

is a square matrix of order $N_t N_r$ representing the virtual array imperfection matrix, $\otimes$ denotes the Kronecker product, and vec$(\cdot)$ vectorization, i.e., stacking the columns of a matrix. As a consequence of the Kronecker product, more model parameters are to be estimated when determining $\mathbf{C}_v$ instead of the transmit and receive imperfection matrices separately.

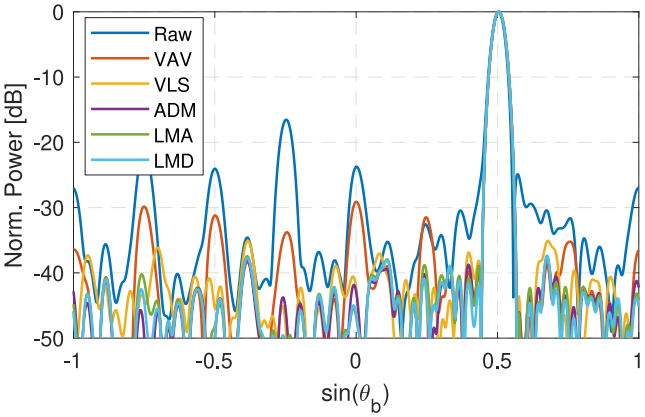

FIGURE 2. Beam pattern of the validation set with a target at $\theta_0 = 30°$ for the selected calibration techniques using all calibration measurements for coefficient estimation.

3) *Angle-Dependent Matrices (ADM):* By utilizing that several coefficient estimations are obtained for each channel and angle, robust angle-dependent coefficients can be acquired [34].
4) *Levenberg-Marquardt All (LMA):* The proposed calibration technique without reduction of model parameters and an initial damping factor set to one. The technique results in a similar performance as the one presented in [25], however, with reduced computational complexity.
5) *Levenberg-Marquardt Diagonal (LMD):* The proposed calibration technique when reducing the number of model parameters and using the same initial damping factor as for LMA. From a full-wave simulation of the antenna array, coupling below -40 dB in amplitude are omitted. On receive, the coefficients r_{nm} reach this level for $|n-m| > 4$ resulting in 12 omitted parameters. On transmit, the coefficients t_{nm} already reach the threshold at $|n-m| > 2$, which reduces the number of model parameters from 64 to 34. Note that this technique is not confined to the channel imbalances in the diagonal. The significant mutual coupling in the subdiagonals is also considered.

Conclusively, 159 sets of calibration coefficients are produced for each of the five techniques from the training set. These are used to independently calibrate all 161 validation measurements ranging from $\theta_0 = \pm 80°$.

C. SIMULATION RESULTS

The beam pattern of the calibrated signal with a point target at $\theta_0 = 30°$ for the five calibration techniques using an FFT beamformer is illustrated in Fig. 2. All calibration measurements in the training set, linearly spaced across the angle span of $\theta_0 = \pm 80°$, are used for the coefficient estimation, such that best performance for all techniques are obtained. The virtual array has been Hamming weighted. Weighting makes the performance more sensitive to calibration errors since the impact of imperfections on

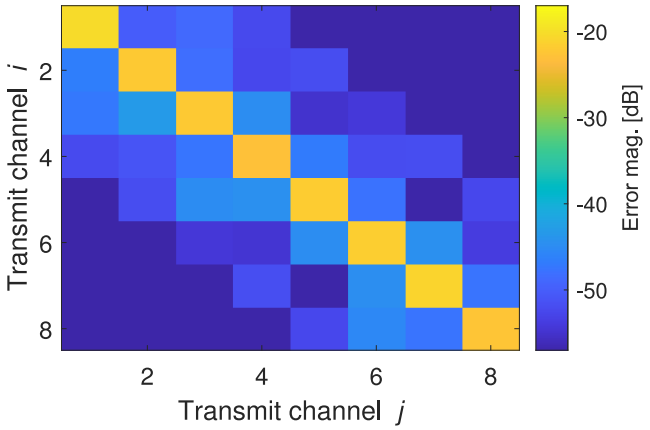

FIGURE 3. The absolute value of the complex difference between the coupling coefficients estimated with LMD and the true coupling coefficients of the transmit array.

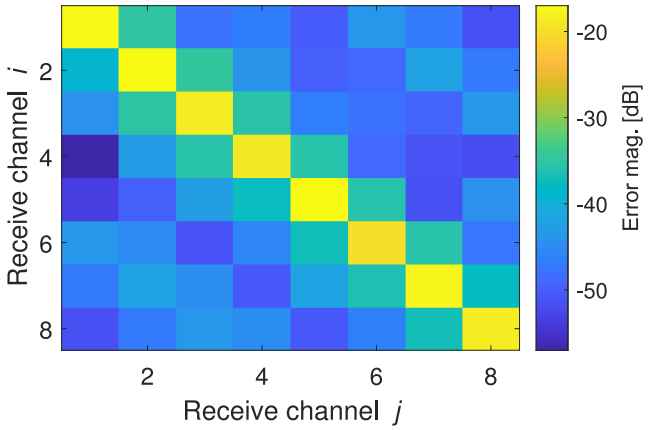

FIGURE 4. The absolute value of the complex difference between the coupling coefficients estimated with LMD and the true coupling coefficients of the receive array.

the sidelobe properties increases. All calibration techniques reduce the PSL, but VAV has the poorest performance. This is also expected as it is the simplest and lightest technique in terms of computational complexity. Otherwise, the other four techniques have comparable performance. The number of iterations for both LMA and LMD is five and seven for the transmit and receive array, respectively, i.e., a total of twelve iterations are realized. However, as the number parameters in (17) is lower for LMD, the computational complexity is also reduced.

High performance is achieved in terms of the sidelobe level. However, as the true coupling matrices are known in a simulation environment, it is possible to evaluate the actual estimated coefficients. Each coefficient in either transmit or receive are evaluated by the amplitude of the complex difference, or for the whole matrix:

$$\delta \mathbf{C}_\alpha = 20 \log_{10}\Big(\Big|\mathbf{C}_\alpha - \hat{\mathbf{C}}_\alpha\Big|\Big), \tag{23}$$

where the logarithm is computed element-wise. For the transmit array, constituting the sparse array, the results are depicted in Fig. 3 for the LMD calibration technique. Most of the diagonal elements lie between -20 and -30 dB, while the off-diagonals elements lie in the region between -50 and -30 dB. As the outer off-diagonals are omitted for LMD, it is reassuring to see that the extremely low differences are achieved which emphasizes the proposed calibration technique.

For the receive array, the estimated coefficients deviate approximately 2–3 dB more from the true values compared to the transmit array as seen in Fig. 4. This is also anticipated as the coupling coefficients are stronger for the full array. Nonetheless, the complex difference for both transmit and receive array lie at least -17 dB below the true value to be estimated.

The PSL when applying the estimated coefficients to the entire validation set is illustrated in Fig. 5. As only the average angle dependency is considered in VAV, the PSL varies up to 5 dB, especially at higher angles. Otherwise,

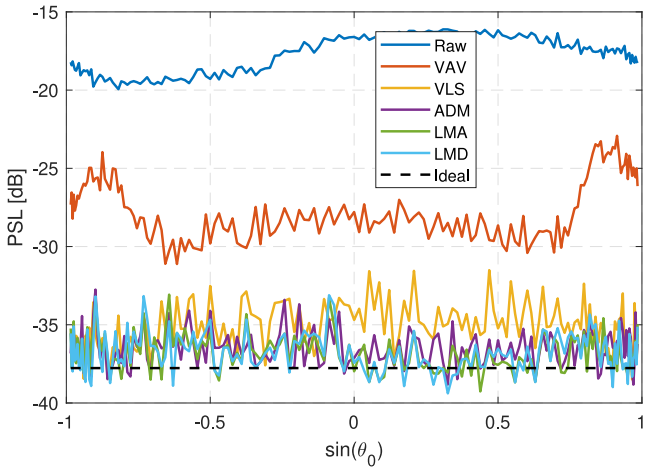

FIGURE 5. Simulated PSL across all validation measurements when applying the selected calibration techniques using all calibration measurements for coefficient estimation.

similar performance tendencies are obtained for all angles, meaning that the angle-dependent effects due to mutual coupling are compensated for. The performance approaches its optimal value of approximately -38 dB in the case of a Hamming-weighted MIMO system with 30 dB SNR. This is in contrast to the -42 dB sidelode level under ideal conditions.

How the average PSL for all 161 validation measurements changes with respect to the number of calibration measurements is depicted in Fig. 6. For VLS, 64 measurements are needed for the matrix inversion. However, 81 calibration measurements are needed to obtain a better PSL than that of VAV. Afterwards, the PSL slowly decreases asymptotically towards -38 dB as the over-fitting of noise is reduced. The required calibration measurements for LMA and LMD are 13 and 10, respectively. To a much smaller degree, LMA suffers from the same problem as VLS, so comparable performance between LMA and LMD is reached when using 35 calibration measurements. Finally, it should be noted that high performance is achieved because all assumptions are

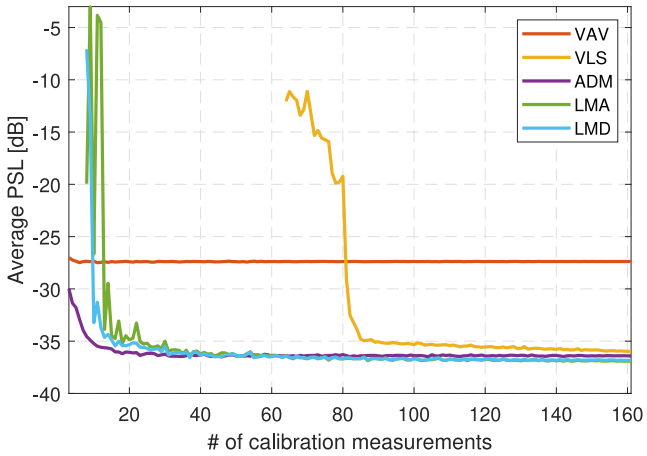

FIGURE 6. Simulated average PSL for all 161 validation angles as a function of measurements used for estimating calibration coefficients.

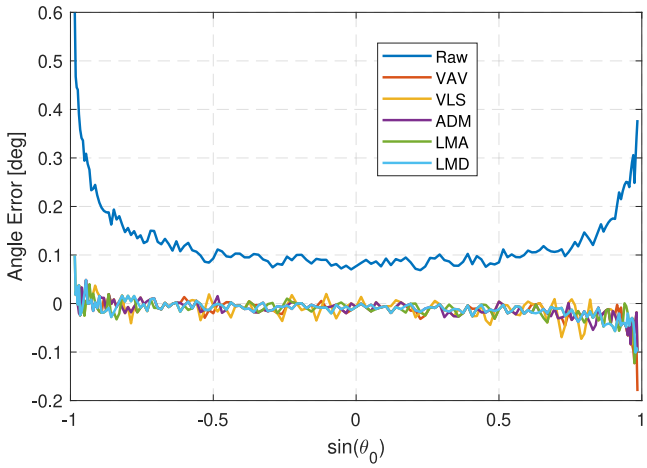

FIGURE 7. Simulated angle error across all validation measurements when applying the selected calibration techniques using all calibration measurements for coefficient estimation.

met, which also explains why ADM does not provide better performance.

Similarly, the angle error has been estimated for the different calibration techniques. Fig. 7 illustrates the angle error for the signal before and after calibration. For all implemented calibration techniques, extremely high accuracy is achieved, and the angle error is quite low even without calibration. Using conventional beamforming, the angular resolution, i.e., the mainlobe width, approximates to

$$\Delta\theta \approx \frac{\lambda}{N_v d \cos\theta} \approx \frac{2}{N_v}\bigg|_{d=\lambda/2,\theta=0} \tag{24}$$

where d is the equidistant inter-element spacing of the full array, and N_v is the number of virtual elements. For $N_v = 64$ the angular resolution becomes roughly 1.8° even without applying a window function. The mainlobe doubles for a Hamming window; thus, the achieved angle error of approximately 0.1° at boresight for the uncalibrated data is much lower than the resolution.

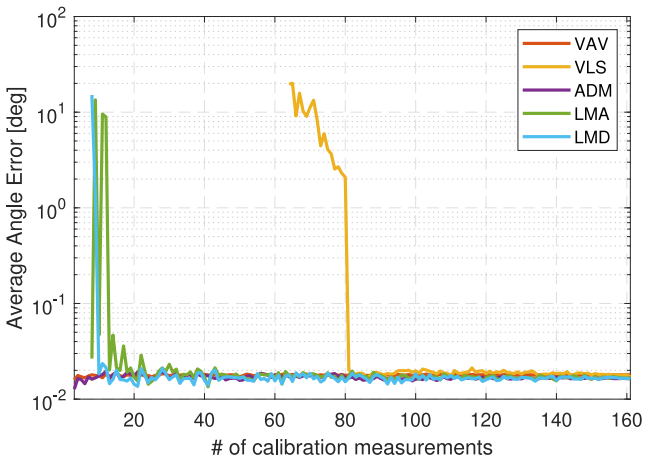

FIGURE 8. Simulated average angle error for all 161 validation angles as a function of measurements used for estimating calibration coefficients.

In Fig. 8, the average angle error is estimated as a function of the number of calibration measurements. The behaviour highly resembles the PSL results, where large angle deviations are observed when an insufficient number of calibration measurements are available. It should be noted that large arrays are less vulnerable to imperfection outliers such that deviations from the true angle are relatively small. In conclusion, the PSL is a preferable performance metric with the given setup.

D. NOISE DISCUSSION

The normalization with a reference channel in (12) and (15) amplifies the noise component and can potentially change the noise shape. Hence, a good SNR is crucial for achieving high calibration performance. Previously, it was found that an SNR of 30 dB indeed accomplishes high performance, and in the following the deterioration of the LMD performance as a function of SNR is assessed numerically.

The simulations described previously have been repeated using all 161 calibration measurements, while varying the SNR between -5 and 30 dB, assuming additive white Gaussian noise. It should be noted that the SNR is after range and Doppler processing, and additional measurement time may be introduced to further increase the SNR in a calibration scenario. For each simulated measurement set, calibration coefficients are estimated using LMD, and the amplitude of the complex difference is computed similar to (23), but for diagonal elements only. Finally, the eight elements are averaged before conversion to dB, which leaves a single scalar for the transmit and receive arrays, evaluating the quality of the estimated calibration matrices.

As illustrated in Fig. 9, the transmit array generally performs better than the receive array by approximately 3 dB. It constitutes the sparse array, where the coupling effects are weaker. With less coupling, the diagonal elements are dominating the coupling matrix, and the angle dependency is reduced, which increases the robustness towards noise. Hence, it is anticipated that the average complex difference is

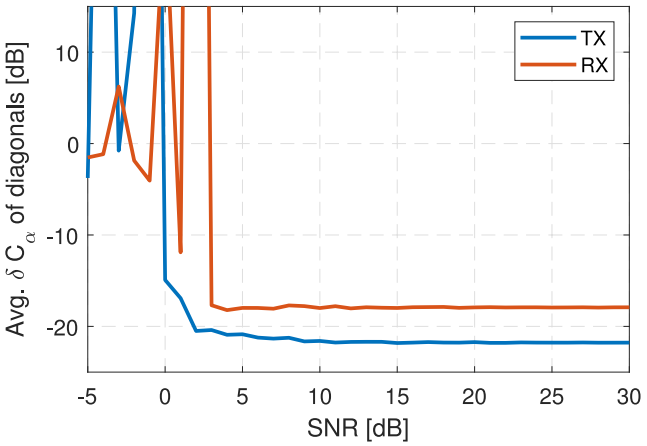

FIGURE 9. Average amplitude of the complex difference between all diagonal elements estimated with LMD and the true values as a function of SNR.

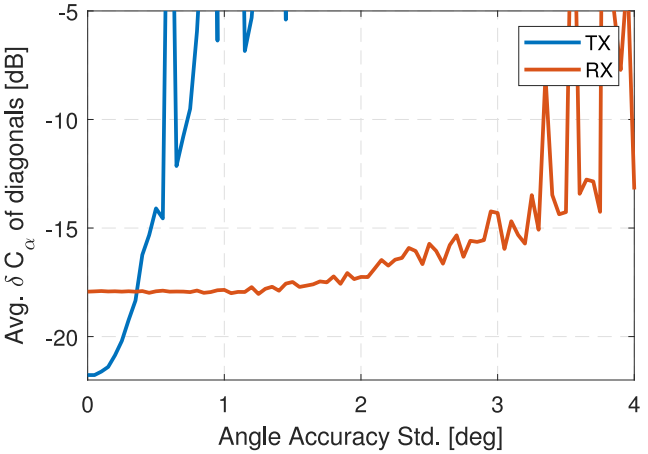

FIGURE 10. Average amplitude of the complex difference between all diagonal elements estimated with LMD and the true values as a function of angle accuracy std.

reasonably constant until the SNR is reduced to 3 dB for the receive array. Here convergence towards a local minimum is obtained and the estimated calibration matrix does no longer reflect the simulated matrix. The same occurs for the transmit array, however, for a lower SNR of 0 dB.

In conclusion, the proposed algorithm is rather unaffected by a reduced SNR, until a certain level, where LMD fails to achieve calibration coefficients matching the true values.

E. ANGLE ACCURACY DISCUSSION

Finally, to model the angle dependency of the antenna arrays, the proposed calibration technique requires multiple measurements at different angles. The minimized values are the measured signal in relation to the ideal signal from a given angle, as described in (17). However, if the DOA does not match with the expected angle relative to the array boresight, an additional source of interference occurs. Naturally, the angle accuracy depends on the equipment available for rotating the radar under test such as a turn table. Hence, it is relevant to investigate how inaccurate angle rotation effects the performance of the calibration algorithm. Again, the performance is assessed using the amplitude of the complex difference between the estimated and the true calibration matrices, averaged across the diagonal elements.

An angle error is added to the true DOA for all 161 measurements that constitutes a single calibration estimation. The applied error follows a zero-mean normal distribution and the standard deviation varies between 0 and 4 degrees. The simulation outcome for both the transmit and receive arrays is illustrated in Fig. 10 for an SNR $= 30$ dB using the proposed LMD calibration technique.

Without any error, the evaluator is -22 and -17 dB for the transmit and receive arrays, respectively. It is also observed, that the receive array is rather unaffected by the angle inaccuracy up to approximately 3 degree standard deviation, where the evaluator has increased approximately 2.5 dB. On the other hand, the transmit array is highly affected by errors of the expected ideal signal. At a std of approximately 0.3 degrees, the transmit and receive arrays are estimated equally well, however at 0.5 degrees the transmit coefficients highly deviates from the true values. This is easily explained by the difference in angle resolution, or also referred to as beamwidth. As the dimensions of the transmit and receive array are 96 and 12 cm, respectively, their approximated beamwidths are 1.8 and 14.3 degrees. In addition, Fig. 10 also illustrates that accurate calibration coefficients under rough conditions can be estimated for one array but not the other, which documents the full separation of the two arrays.

In conclusion, the robustness of the calibration technique depends highly on the beamwidth. For smaller arrays, either by a limited number of antenna elements or for a two-dimensional array without any sparse array, the requirement of high angle accuracy is not as demanding.

V. EXPERIMENTAL VERIFICATION

To attain performance estimates of an actual system, the proposed calibration technique has been applied to a MIMO radar demonstrator designed and built for drone detection at DTU Space [27].

A. EXPERIMENTAL SETUP

The antenna array is depicted in Fig. 11. Similar to the simulated MIMO system, it consists of an 8×8 antenna array resulting in a 64-element virtual ULA with $\lambda/2$ spacing and a carrier frequency of 9.4 GHz. Furthermore, the training and validation sets are measured with targets located at $\theta_0 = [-80°, 80°]$ and an angle separation of one degree.

Precautions are applied to the measurement setup to accommodate for all assumptions listed in Section II:

a) The measurements are conducted in an anechoic chamber to reduce clutter. Two dominating effects of performing the calibration measurements in an anechoic chamber are described in [35] including the correction necessitated by the near-field propagation

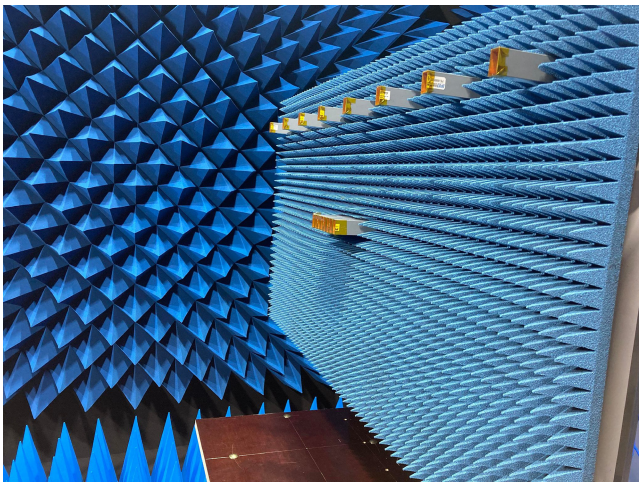

FIGURE 11. The antenna array of the MIMO radar used for calibration validation inside the anechoic chamber in which the calibration measurements were performed.

conditions. With a target range of 7 meters, it is far below the far-field range of approximately 50 m, and accordingly, near-field phase corrections are applied prior to the beamforming and coefficient estimation. In the near-field, the perceived DOA-angles of all elements are different, and amplitude variations caused by the radiation pattern occur. These are however negligible for this experimental setup.

b) A corner reflector is used as calibration target to resemble a single point target.

c) On top of reducing clutter by conducting the measurements in an anechoic chamber, background subtraction is performed. This is implemented by collecting a data set of the background signal without the corner reflector at the same angles as the training and validation set. The complex, raw signal of the background data set is then subtracted from the two other data sets. This also suppresses the direct coupling between transmit and receive.

d) Alternating time-division multiplexing is applied for complete orthogonality where only a single transmit antenna radiates at a time. In addition, linear frequency-modulated waveforms are used with a bandwidth of 200 MHz.

e) Identical open-ended waveguide antennas are used across the entire array. Moreover, their FOV is approximately $\pm 60°$, which justifies validating the calibration algorithm across a large angle span of $\pm 80°$.

f) According to [30], open-ended waveguides are not perfect MSAs. Hence, performance degradation is expected compared to the simulated scenario.

g) The antenna aperture x and y coordinates from Fig. 1 is centred at the turn table origin, which can roughly be seen in Fig. 11.

For an experimental setup, the actual DOA of the target relative to the antenna array, θ_0, also has a finite accuracy. With the radar centered at the turntable origin, they arise from either a displacement between the radar and the corner reflector or simply from the turn table angle accuracy. Besides measuring the geometry of the experimental setup as accurately as possible, the DOA estimates from the uncalibrated system are used to verify the actual DOA. The expected angle error is much lower than the angular resolution and comparable to the measurement inaccuracy. Hence, it will not be evaluated using the MIMO radar demonstrator.

B. EXPERIMENTAL RESULTS

An example of the PSL across all validation measurements with and without calibration is illustrated in Fig. 12 using all calibration measurements in the training set. For all calibration techniques except ADM, the PSL are higher than their simulation counterparts in Fig. 5, including the PSL of the uncalibrated signal, which is approximately 5 dB higher. These observations indicate more significant system imperfections and deviations from the system and environment assumptions. Furthermore, considerable PSL variations across θ_0 are observed for the techniques with few model parameters, especially for the larger DOA angles where the performance tends to decrease.

The estimation of PSL is repeated for different numbers of calibration measurements, and averaged across all validation measurements resulting in Fig. 13. For all calibration techniques, the same tendencies are seen as for the simulated scenario. However, for LMA and LMD, the number of required calibration measurements to consistently outperform VAV is 15 and 35, respectively. This is a significant increase in measurements, for LMA in particular. Furthermore, the PSL obtained is worse for all implemented algorithms. Using all 161 training measurements, the PSL deteriorates only by 2 dB for ADM, 5 dB for VAV and VLS, and approximately 8 dB for both LMA and LMD. Consequently, VLS outperforms the simpler models when enough data is provided in terms of PSL.

This is an evident indication that the antennas are indeed not MSAs: As the coupling matrix is angle-dependent, ADM is unaffected by the non-MSA impact on the system, while VLS profits from having unnecessarily many model parameters to compensate for the effects. On the contrary, LMA and LMD with a more appropriate number of model parameters relative to the physical system, cannot describe the non-MSA impacts to the same extent.

On top of the increased computational complexity, the need for more than 80 calibration measurements is often cumbersome or time-consuming. Hence, even if the antenna system consists of non-MSAs, it would be appropriate to implement a calibration technique that reduces the measurement count. LMD, being less computationally complex while achieving better PSL with considerably fewer measurements, outperforms LMA and verifies the calibration capability.

A performance degradation is observed for the large angles. Hence, it is of interest to quantify the effect of

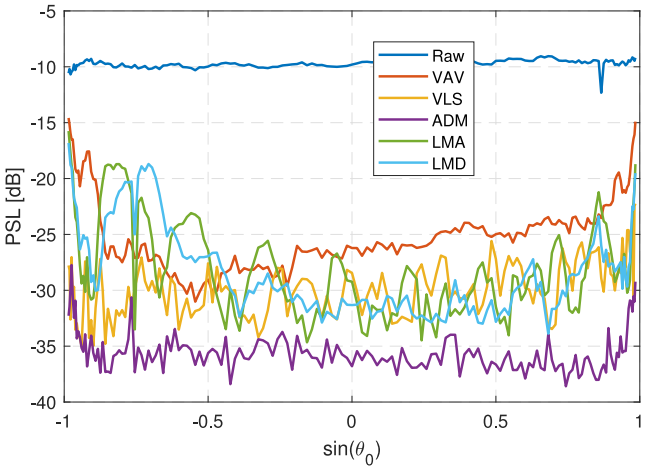

FIGURE 12. Example of PSL across all validation angles for the different calibration techniques using all 161 measurements for coefficient estimation.

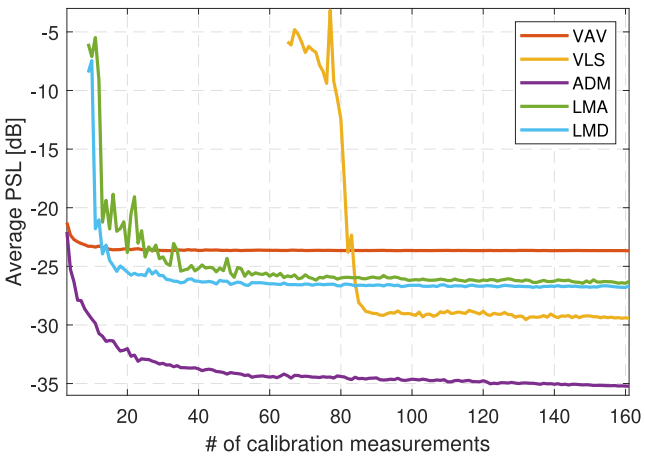

FIGURE 13. Average PSL for all 161 validation angles as a function of measurements used for estimating calibration coefficients.

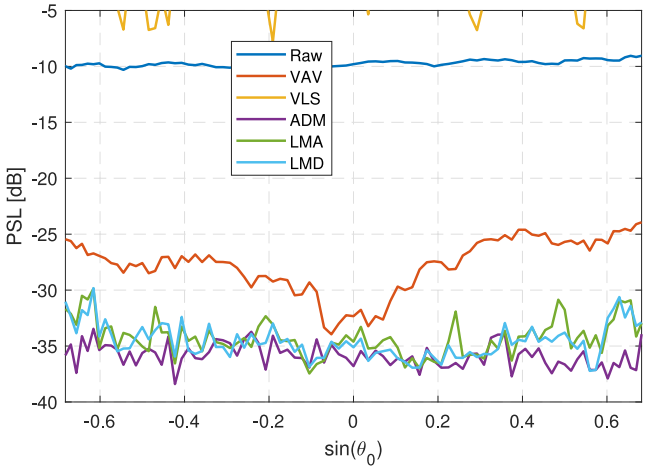

FIGURE 14. Example of PSL across the validation angles in the interval ±45° for the different calibration techniques using the 91 measurements of the training set for coefficient estimation.

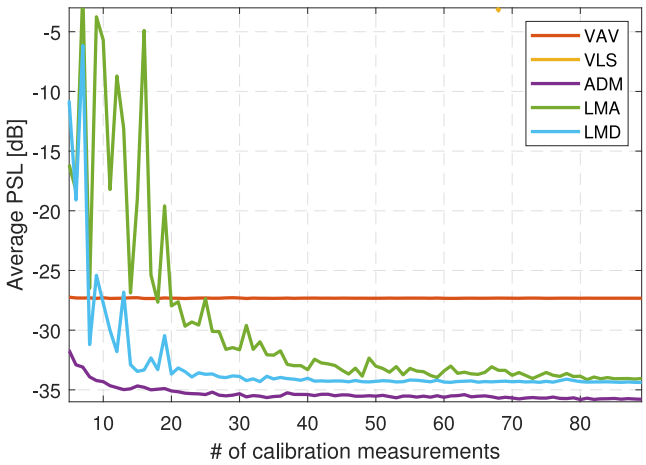

FIGURE 15. Average PSL for the selected 91 validation angles as a function of measurements used for estimating calibration coefficients.

the antennas not being MSAs by applying the calibration techniques to a reduced FOV of ±45°. Maintaining the angle separation of one degree, 91 measurements of the training set are used. Applying the new set of coefficients to the corresponding validation data results in the PSL values illustrated in Fig. 14. The first observation standing out is that VLS has not found a least squares solution describing the system such that no well-defined point target is obtained after beamforming. When limiting the angle span of the training set, the variations across each measurement also decreases, making it more challenging to estimate the coefficients that describe the existing system. On the other hand, the limited angle span improves the performance of VAV as fewer variations due to the angle dependency results in a better approximation when averaging. Comparing Fig. 12 and Fig. 14, the reduction of the non-MSA effects on the beam pattern is seen to considerably improve the PSL of LMA and LMD, which is approaching the performance of ADM.

Finally, in Fig. 15 the average PSL across all angles in the ±45° interval is computed for several number of calibration measurements extracted from the training set within the same interval. Even though the average PSL of VAV has improved by approximately 5 dB, both LMA and LMD outperform VAV with even fewer measurements compared to when using the full training data set. An improved PSL is achieved with LMD compared to LMA until the full training set is used, where the PSL is almost identical. It should be noted that a high LMD performance is already achieved with $Q = 8$, which is possible due to the model parameter reduction. More specifically, 54 equations are available to estimate 52 parameters from the array where fewest model parameter are removed.

VI. CONCLUSION

In this paper, a novel calibration technique for a colocated MIMO radar system is presented and applied to data from a simulation environment and a demonstrator. Two versions of

the technique are presented, as model parameter reduction can be implemented in case some coupling coefficients are negligible. For both versions, high calibration performance is obtained in terms of deviations from the ideal imperfection matrices simulated and a low PSL computed with simulated and measured radar data. This is achieved with few calibration measurements and low computational complexity regarding the number of model parameters to estimate and iterations for the nonlinear least squares. For the 8×8 MIMO demonstrator, the number of model parameters to estimate is reduced from 128 to 86 without observing any drawbacks. On the contrary, half as many measurements are needed to reach an adequate average sidelobe level across all angles with parameter reduction. Higher sidelobes are observed for larger angles when applying the proposed calibration technique to the demonstrator data, primarily as a result of the minimum scattering antenna approximation not being entirely met. Finally, it was found that limiting the angular interval of the calibration measurements, the irregularities caused by the non-minimum scatterers are highly circumvented resulting in the proposed method being the one with best performance.

REFERENCES

[1] J. Li and P. Stoica, *MIMO Radar Signal Processing*. New York, NY, USA: Wiley, 2008.

[2] F. Belfiori, W. Van Rossum, and P. Hoogeboom, "Coherent MIMO array design with periodical physical element structures," *IEEE Antennas Wireless Propag. Lett.*, vol. 10, pp. 1341–1344, 2011.

[3] J. Li and P. Stoica, "MIMO radar with colocated antennas," *IEEE Signal Process. Mag.*, vol. 24, no. 5, pp. 106–114, Sep. 2007.

[4] R. Feger, C. Wagner, S. Schuster, S. Scheiblhofer, H. Jager, and A. Stelzer, "A 77-GHz FMCW MIMO radar based on an SiGe single-chip transceiver," *IEEE Trans. Microw. Theory Techn.*, vol. 57, no. 5, pp. 1020–1035, May 2009.

[5] A. Ganis et al., "A portable 3-D imaging FMCW MIMO radar demonstrator with a 24 × 24 antenna array for medium-range mapplications," *IEEE Trans. Geosci. Remote Sens.*, vol. 56, no. 1, pp. 298–312, Jan. 2018.

[6] S. Sun, A. P. Petropulu, and H. V. Poor, "MIMO radar for advanced driver-assistance systems and autonomous driving: Advantages and challenges," *IEEE Signal Process. Mag.*, vol. 37, no. 4, pp. 98–117, Jul. 2020.

[7] J. Klare, O. Biallawons, and D. Cerutti-Maori, "Detection of UAVs using the MIMO radar MIRA-CLE Ka," in *Proc. EUSAR: 11th Eur. Conf. Synthetic Aperture Radar*, 2016, p. 7559402.

[8] F. Yang, F. Xu, F. Fioranelli, J. Le Kernec, S. Chang, and T. Long, "Practical investigation of a MIMO radar system capabilities for small drones detection," *IET Radar Sonar Navig.*, vol. 15, no. 7, pp. 760–774, 2021.

[9] R. Grove and J. Dall, "On the impact of channel imbalance on MIMO radar performance," in *Proc. 17th Eur. Radar Conf. (EuRAD)*, 2021, pp. 300–333.

[10] M. Eschbaumer, "Impact of channel imbalances on beamforming performance in automotive MIMO radar," in *Proc. 18th Eur. Radar Conf. (EuRAD)*, 2021, pp. 525–528.

[11] B. T. Arnold and M. A. Jensen, "The effect of antenna mutual coupling on MIMO radar system performance," *IEEE Trans. Antennas Propag.*, vol. 67, no. 3, pp. 1410–1416, Mar. 2019.

[12] C. M. Schmid, S. Schuster, R. Feger, and A. Stelzer, "On the effects of calibration errors and mutual coupling on the beam pattern of an antenna array," *IEEE Trans. Antennas Propag.*, vol. 61, no. 8, pp. 4063–4072, Aug. 2013.

[13] B. Clerckx, C. Craeye, D. Vanhoenacker-Janvier, and C. Oestges, "Impact of antenna coupling on 2 x 2 MIMO communications," *IEEE Trans. Veh. Technol.*, vol. 56, no. 3, pp. 1009–1018, May 2007.

[14] E. Christensen et al., "EMISAR: An absolutely calibrated polarimetric L- and C band SAR," *IEEE Trans. Geosci. Remote Sens.*, vol. 36, no. 6, pp. 1852–1865, Nov. 1998.

[15] TI. "Self-calibration in TI's mmWave radar devices." Accessed: Mar. 1, 2023. [Online]. Available: https://www.ti.com/lit/an/spracf4b/spracf4b.pdf?ts=1672737012570

[16] H. Steyskal and J. Herd, "Mutual coupling compensation in small array antennas," *IEEE Trans. Antennas Propag.*, vol. 38, no. 12, pp. 1971–1975, Dec. 1990.

[17] G. Babur, P. J. Aubry, and F. Le Chevalier, "Antenna coupling effects for space-time radar waveforms: Analysis and calibration," *IEEE Trans. Antennas Propag.*, vol. 62, no. 5, pp. 2572–2586, May 2014.

[18] D. Bleh et al., "W-band time-domain multiplexing FMCW MIMO radar for far-field 3-D imaging," *IEEE Trans. Microw. Theory Techn.*, vol. 65, no. 9, pp. 3474–3484, Sep. 2017.

[19] F. Belfiori, W. Van Rossum, and P. Hoogeboom, "Array calibration technique for a coherent MIMO radar," in *Proc. 13th Int. Radar Symp.*, 2012, pp. 122–125.

[20] K. R. Dandekar, H. Ling, and G. Xu, "Experimental study of mutual coupling compensation in smart antenna applications," *IEEE Trans. Wireless Commun.*, vol. 1, no. 3, pp. 480–487, Jul. 2002.

[21] I. J. Gupta, J. R. Baxter, S. W. Ellingson, H. G. Park, H. S. Oh, and M. G. Kyeong, "An experimental study of antenna array calibration," *IEEE Trans. Antennas Propag.*, vol. 51, no. 3, pp. 664–667, Mar. 2003.

[22] M. Mowler and B. Lindmark, "Estimation of coupling, element factor, and phase center of antenna arrays," in *Proc. IEEE Antennas Propag. Soc. Int. Symp.*, vol. 4, 2005, p. 1552724.

[23] C. M. Schmid, C. Pfeffer, R. Feger, and A. Stelzer, "An FMCW MIMO radar calibration and mutual coupling compensation approach," in *Proc. Eur. Radar Conf.*, 2013, pp. 13–16.

[24] A. Durr et al., "On the calibration of mm-Wave MIMO radars using sparse antenna arrays for DOA estimation," in *Proc. 16th Eur. Radar Conf.*, 2019, pp. 349–352.

[25] Z. Jianxiong, Z. Rongqiang, and L. Haorun, "Mutual coupling compensation for compact MIMO radar," *IEEE Trans. Antennas Propag.*, vol. 70, no. 7, pp. 6018–6023, Jul. 2022.

[26] Z. Li, Y. Zhang, S. Zhang, and X. Zhang, "Independent transmit and receive channel calibration for multiple-input multiple-output (MIMO) systems," U.S. Patent 368 388 A1, Nov. 17, 2022.

[27] R. Grove, "MIMO radar systems and algorithms, imperfections and calibration," Ph.D. dissertation, DTU Space Dept., Technical Univ. Denmark, Kongens Lyngby, Denmark, 2022.

[28] H. Sun, F. Brigui, and M. Lesturgie, "Analysis and comparison of MIMO radar waveforms," in *Proc. Int. Radar Conf.*, 2014, pp. 1–6.

[29] W. Kahn and H. Kurss, "Minimum-scattering antennas," *IEEE Trans. Antennas Propag.*, vol. AP-13, no. 5, pp. 671–675, Sep. 1965.

[30] J. B. Andersen and A. Frandsen, "Absorption efficiency of receiving antennas," *IEEE Trans. Antennas Propag.*, vol. 53, no. 9, pp. 2843–2849, Sep. 2005.

[31] D. Kelley and W. Stutzman, "Array antenna pattern modeling methods that include mutual coupling effects," *IEEE Trans. Antennas Propag.*, vol. 41, no. 12, pp. 1625–1632, Dec. 1993.

[32] D. Pozar, "The active element pattern," *IEEE Trans. Antennas Propag.*, vol. 42, no. 8, pp. 1176–1178, Aug. 1994.

[33] D. Pozar, "A relation between the active input impedance and the active element pattern of a phased array," *IEEE Trans. Antennas Propag.*, vol. 51, no. 9, pp. 2486–2489, Sep. 2003.

[34] R. Grove, J. Dall, and P. Leth-Espensen, "Mutual coupling and channel imbalance calibration of colocated MIMO radars," *IEEE Open J. Antennas Propag.*, vol. 3, pp. 511–522, 2022.

[35] D. Raphaeli and I. Bilik, "Challenges in automotive MIMO radar calibration in anechoic chamber," *IEEE Trans. Aerosp. Electron. Syst.*, vol. 59, no. 5, pp. 6205–6214, Oct. 2023.

RICARD L. GROVE received the M.S. degree in electrical engineering within the earth and space physics and engineering program from the Technical University of Denmark, Kongens Lyngby, Denmark, in 2017, and the Ph.D. degree in radar signal processing from the Technical University of Denmark in 2022, after which he continued his research within system imperfections, such as channel imbalance and mutual coupling in MIMO radars until 2023. He is currently with Weibel Scientific A/S as a Radar Signal Processing and Software Engineer.

JØRGEN DALL (Member, IEEE) received the M.Sc. degree in electrical engineering and the Ph.D. degree from the Technical University of Denmark in 1984 and 1989, respectively, where he is a Professor of Microwave Remote Sensing Systems. He has contributed to the development of the Danish airborne SAR, EMISAR, notably he led the development of a dedicated real-time SAR processor, was responsible for the offline data processing, and organized the EMISAR data acquisition campaigns in a five-year period. Later, he led the development of ESA's airborne Ice Sounding radar and SAR, POLARIS. Most recently he led the development of an experimental X-band MIMO radar. His research interests include various aspects of ice sheet mapping using InSAR, PolInSAR, and TomoSAR techniques as well as radar ice sounding.